Article



Coarse-Grained Modeling of Pore Dynamics on the Red Blood Cell Membrane under Large Deformations

Meghdad Razizadeh, Mehdi Nikfar, Ratul Paul, and Yaling Liu^{1,2,*}

Department of Mechanical Engineering and Mechanics and Department of Bioengineering, Lehigh University, Bethlehem, Pennsylvania

ABSTRACT Transient pore formation on the membrane of red blood cells (RBCs) under high mechanical tensions is of great importance in many biomedical applications, such as RBC damage (hemolysis) and mechanoporation-based drug delivery. The dynamic process of pore formation, growth, and resealing is hard to visualize in experiments. We developed a mesoscale coarse-grained model to study the characteristics of transient pores on a patch of the lipid bilayer that is strengthened by an elastic meshwork representing the cytoskeleton. Unsteady molecular dynamics was used to study the pore formation and reseal at high strain rates close to the physiological ranges. The critical strain for pore formation, pore characteristics, and cytoskeleton effects were studied. Results show that the presence of the cytoskeleton increases the critical strain of pore formation and confines the pore growth. Moreover, the pore recovery process under negative strain rates (compression) is analyzed. Simulations show that pores can remain open for a long time during the high-speed tank-treading induced stretching and compression process that a patch of the RBC membrane usually experiences under high shear flow. Furthermore, complex loading conditions can affect the pore characteristics and result in denser pores. Finally, the effects of strain rate on pore formation are analyzed. Higher rate stretching of membrane patch can result in a significant increase in the critical areal strain and density of pores. Such a model reveals the dynamic molecular process of RBC damage in biomedical devices and mechanoporation that, to our knowledge, has not been reported before.

SIGNIFICANCE This work focuses on a coarse-grained model of large membrane patches that includes cytoskeleton structures. We aim to study the dynamic process of pore formation on the red blood cell surface, which is hard or impossible to visualize in experiments. We studied the effects of the cytoskeleton on the critical strain of pore formation and pore characteristics. Moreover, we analyzed the dynamic process of pore reseal, the effects of non-equibiaxial loading conditions, and the time dependence of pore formation. Our results provide new, to our knowledge, insights into the underlying pore formation process that is important in many biomedical applications such as red blood cell damage (hemolysis), mechanoporation-based drug delivery, and further development of multiscale predictive models.

INTRODUCTION

Mechanoporation, pore formation on biological membranes by mechanical stresses, shows significant potential as a loading method in drug delivery systems (1–3). On the other hand, hemolysis—hemoglobin release from red blood cells (RBCs) in medical devices—usually happens through nanoscale pores that are larger than hemoglobin molecules and transiently opened at high-sheared regions (4–8). Classic experimental works reported a critical shear rate

of 42,000 s⁻¹ (6% of areal strain) for the lysis of RBCs under steady shear flow (9). Modeling of hemolysis is usually performed by macroscale stress- or strain-based methods (6,10). In stress-based models, the hemolysis is calculated by empirical equations fitted to experimentally measured free hemoglobin concentrations in the blood based on the applied shear stress and total exposure time (11,12). Strain-based models utilize global strains of RBCs to find the index of hemolysis based on the deformations applied on each RBC (13,14). However, the physics of pore formation and release of hemoglobin molecules are not considered in the above-mentioned models, and results are dependent on the specific device that is under study. To address this issue, Vitale et al. (15) developed a multiscale approach in

Submitted February 17, 2020, and accepted for publication June 16, 2020.

*Correspondence: yal 310@lehigh.edu

Editor: Ana-Suncana Smith.

https://doi.org/10.1016/j.bpj.2020.06.016

© 2020 Biophysical Society.



which the sublytic damage of RBC is quantified by global strains of each RBC and pore characteristics which are estimated based on a theoretical model of the membrane energy landscape. Another multiscale damage model based on the local strains on each patch of RBC was developed by Sohrabi and Liu (5). In that model, the hemolysis is calculated locally on each patch of an RBC triangular network model by comparing the local areal strains with the probability of pore formation and pore characteristics based on allatomistic (AA) and coarse-grained molecular dynamics (CGMD) simulations. However, the cellular-scale local strain criteria such as strain rate, patch size, and loading conditions were not similar to the lower-scale AA and CGMD models employed to calculate pore characteristics. This can be considered as one of the major error sources in that multiscale approach. Therefore, understanding subcellular mechanisms of pore formation, growth, and closure on the surface of RBC membrane is important for hemolysis and many other biomedical applications. Characterization of the pore formation process is challenging because of its multiscale and dynamic nature. The diameter of erythrocytes is $\sim 8 \mu m$, which is almost three orders of magnitude larger than nanoscale pores transiently formed on the membrane surface to transport molecules with a size of a few tens of nanometers. Therefore, multiscale approaches that are able to both model the microscale deformations (finiteelement or spring-connected network methods to model RBCs) and nanoscale pore formation and resealing (molecular dynamics simulations) at their relevant timescales are highly demanded (16,17). Although many numerical methods have been developed to model RBC deformations in fluid flow, the process of formation, growth, and resealing of large nanopores (large enough to allow diffusion of large molecules such as hemoglobin) is yet to be understood.

During the last two decades, in silico molecular dynamics simulations have been widely used to study pores in biological membranes (18–26). AA simulations provide valuable insights into the free energy (18-20,22), critical areal strain (21), and underlying atomistic mechanisms of pore formation (18,19) and reseal (26). However, the accessible time- and size scales are limited by the high computational costs. Therefore, the dynamics of the pore formation process can only be studied at unrealistically high stretching velocities (0.025-30 m/s (23)), which dramatically affects the time-dependent phenomenon of pore formation (27). Moreover, in moderate surface tensions, the timescale of pore formation in intact membranes is longer than the accessible range of AA simulations. Therefore, the dynamics of pore formation in healthy (without preformed pores) AA lipid membranes can only be studied at high surface tensions, in the range of 90 mN/m (-200 bar lateral tension (19)). High strain rates and finite-size effects of AA simulations result in the overestimation of critical strains by two orders of magnitude. Although the micropipette aspiration experiments show that RBCs cannot withstand areal strains of more than 4% (27,28), in AA simulations, the lipid membrane is able to be stretched up to 200% (23). To increase the accessible time- and length scales and simulate more realistic membranes, many CGMD methods have been developed. Marrink et al. (29) employed the MARTINI CGMD method and reported the same qualitative process of pore formation as AA simulations. They also showed that pores will be formed in membranes at the surface tension of 65 mN/m on a timescale of several microseconds. In addition to chemical-specificity-preservative coarse-graining methods, by utilizing coarser models that use fewer beads to represent lipid molecules, several approaches have been proposed to push the available time- and length scales even further (30–35). Tolpekina et al. (36,37) employed the explicit-solvent CGMD model of Goetz and Lipowski (31) to study the pore nucleation free energy and system size dependence of preformed pores and established a phase diagram for stable, metastable, and unstable pores. They also developed a theoretical model for the size dependency of the pore formation. However, their model does not include the time dependency of the pore formation process. The dependency of critical pore formation strain on the applied loading rate has been reported both by experimental (27,38) and numerical (23,24,39) studies. The implicit-solvent, head-tail model of Cooke et al. (34) is another mesoscale approach that was successfully used to model the lipid membrane mechanical properties and pore formation (34,40,41). By stretching the computational box in a quasistatic way, Deserno (41) reported a critical surface tension of 8 mN/m, which is closer than other simulations to the range of 3-4 mN/m from the experimental results (42,43).

The RBC's extraordinary mechanical properties, such as large deformability and shear stress endurance, are mainly due to its spectrin-actin cytoskeleton structure. Recent super-resolution microscopy results reported the junction-tojunction distance (JD) of \sim 80 nm for the triangular spectrin network (44). To simulate the mechanical properties of the RBC membrane and the interactions between the lipid bilayer and cytoskeleton, Li and Lykotrafitis (45) developed a two-component model that explicitly models the cytoskeleton particles. In their approach, each lipid molecule is modeled by just one bead that interacts with other lipid particles by an orientational potential. One-particle-thick models can be tuned to successfully simulate the self-assembly of lipid molecules into vesicles or bilayers (46,47), and they are coarse enough to simulate large patches of membrane and even whole cells with the cytoskeleton particles (48,49). However, they are limited in terms of analyzing pore formation. The main reason is that in one-particle-thick models, the amphiphilic behavior of lipid molecules is not explicitly simulated with corresponding particles and is modeled by orientational potentials with a favorable minimal potential instead. Therefore, these models cannot capture the accurate dynamics of pore formation from hydrophobic voids to hydrophilic pores. To incorporate more fine-scale details, Spangler et al. (50) used a head-tail lipid model with a simplified cytoskeleton model to study the phase behavior and kinetics of blebbing. They used a triangular elastic meshwork coupled with the lipid bilayer at junction points to represent the cytoskeleton. A similar approach has been utilized by Gao et al. (51) and Sikder et al. (52) to analyze cytoskeleton effects on the endocytosis process and domain formation in biomembranes.

In this work, an implicit-solvent, head-tail representation of lipid bilayer along with a simplified cytoskeleton model are employed to investigate the process of pore formation, growth, and recovery in the RBC membrane under mechanical strains. We analyzed the effects of cytoskeleton and transmembrane proteins (junction structures) in pores formation and growth. Then, the pore recovery is studied for a patch under negative (compressional) strain rates. Moreover, we investigated the effects of complex loading conditions and strain rate on the critical strain of pore formation and other pore characteristics. Although the membrane model and loading conditions are significantly simplified versions of reality, this approach provides a quantified insight into the influence of various parameters on the pore formation process. This can be considered as a first step toward developing a multiscale approach to predict the damage by coupling the cellular-scale deformations and strains with the mesoscale CGMD model of an RBC membrane patch.

METHODS

We utilized the implicit-solvent, head-tail model of Cooke, Kremer, and Deserno (34) to model the lipid bilayer. This model has been widely used to study various problems in the field of biomembranes. Each lipid molecule is made of one head (H) and two tail (T) particles (FT and ST represent first and second tail particles, respectively). All nonbonded interactions are governed by the Weeks-Chandler-Anderson potential given by Eq. 1:

$$v(r) = \begin{cases} 4\varepsilon \left[\left(\frac{\sigma}{r}\right)^{12} - \left(\frac{\sigma}{r}\right)^{6} + \frac{1}{4} \right] & r \le r_{c} \\ 0 & r > r_{c} \end{cases}$$
(1)

in which the ε and σ are energy and length units, respectively; r is the distance between two particles; and r_c is the critical distance, which is $r_c = 2^{1/6}\sigma$. In accordance with the original work of Cooke and colleagues, we set $\sigma_{H-H} = \sigma_{H-T} = 0.95\sigma$ and $\sigma_{T-T} = \sigma$ to ensure the cylindrical shape of lipid molecules. In addition to the above repulsive potential, tail particles interact with each other by a tunable attractive potential of the form Eq. 2:

$$v_{att}(r) = \begin{cases} -\varepsilon & r < r_c \\ -\varepsilon \cos^2\left(\frac{\pi(r - r_c)}{2w_c}\right) & r_c \le r \le r_c + w_c . \end{cases}$$
 (2)

 w_c is the cohesive range of tail particles, which is the main tunable parameter of the model. This parameter is set to get the phase behavior

and self-assembly of the lipid bilayer. The lipid particles are also bonded to each other by an FENE bond of the form Eq. 3:

$$v_{bond}(r) = -\frac{1}{2}k_{bl}r_0^2ln\left(1 - \left(\frac{r}{r_0}\right)^2\right),$$
 (3)

in which $k_{bl} = 30e/\sigma^2$ is the bond constant and r_0 is the maximal extent of the bond, which is $r_0 = 1.5\sigma$. The lipid molecule is also straightened by a harmonic angular potential of the form Eq. 4:

$$v_{bend}(\theta) = \frac{1}{2}k_{al}(\theta - \pi)^2, \tag{4}$$

with $k_{al} = 10\varepsilon/rad^2$ and θ being the angle between the vectors made by H-FT and FT-ST particles. To ensure the fluid-like behavior and flat bilayer shape of membrane, we chose $w_c = 1.6\sigma$ for all simulations. Similar to the works of Spangler et al. (50), Sikder et al. (52), and Gao et al. (51), a triangular meshwork of coarse-grained beads is used to explicitly simulate the cytoskeleton. In this simplified model, the transmembrane proteins are modeled by bolalipid-like junction structures that connect the lipid bilayer to the cytoskeleton. Each bolalipid molecule is made of six particles: two hydrophilic particles located at the two ends (bolalipid head particles: BHs) and four hydrophobic particles in the middle section (bolalipid middle particles: BMs). The nonbonded interactions of bolalipid head and middle particles (BH-BM, BH-BH, and BM-BM) are similar to lipid head and tail particle interactions. However, a simple Lennard-Jones potential is used between lipid head and bolalipid head particles (BH-H), as well as lipid tail and bolalipid middle particles (BM-T). This potential ensures that the junction structures will remain in the lipid bilayer and diffuse with the lipid molecules. Bolalipid particles are also bonded to each other with the harmonic bond, which is given by Eq. 5:

$$v_{bond}(r) = \frac{1}{2}k_{bb}(r - r_0)^2,$$
 (5)

in which the bond constant is $k_{bb} = 100\varepsilon/\sigma^2$ and equilibrium distance is $r_0 =$ σ . Moreover, a harmonic angular potential of the form of Eq. 4 is used with the constant $k_{ab} = 100\varepsilon/rad^2$ to keep the structure straight. Different experimental approaches suggested various numbers in a wide range of 25-200 nm for the junction-to-junction distance (JD) of the human RBC cytoskeleton (53–56). However, recent supermicroscopy results of Pan et al. (44) reported that JD is 80 nm, which is consistent with the length of relaxed spectrin tetramers. Therefore, the JD of triangular meshwork in our model is chosen to be 80σ with 79 beads between two junction points (this setup will be referred to as D80 in the rest of the study). The nonbonded interactions of the cytoskeleton with all other particles are governed by Eq. 1, with $\varepsilon_c = \varepsilon$ and $\sigma_c = \sigma$. The cytoskeleton beads are also connected and straightened by harmonic bonds and angles with the form of Eqs. 4 and 5, with the bond coefficient, $k_{bc} = 100e/\sigma^2$, equilibrium distance of $r_0 = \sigma$, and $k_{ac} =$ ε/rad^2 . The cytoskeleton and bolalipid structures in the lipid bilayer are connected to each other at the cytoskeleton junction points by an unbreakable harmonic bond with the constant of $k_{bj} = 100\varepsilon/\sigma^2$. Fig. 1 shows snapshots of our CGMD model, computational box, and a hydrophilic pore on the membrane surface.

To increase the computational efficiency and simulate membranes that include large cytoskeleton units, we utilized an implicit-solvent model in this work. Solvent molecules can affect the pore formation process, especially through their interactions with hydrophobic parts of lipid molecules during pore nucleation. In the implicit-solvent model of Cooke and Deserno (33), the hydrophobic interactions are modeled by lipid tail-tail attractive potentials. We acknowledge that this simplification might be a source of error in our simulations. However, as reported by Cooke et al. (40), the results of the aforementioned implicit-solvent head-tail model can be perfectly fitted into the model of Tolpekina et al. (37), which

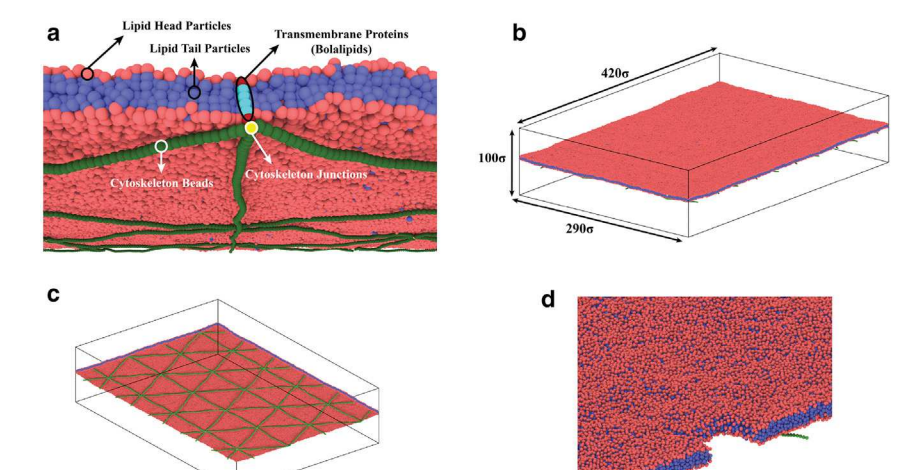
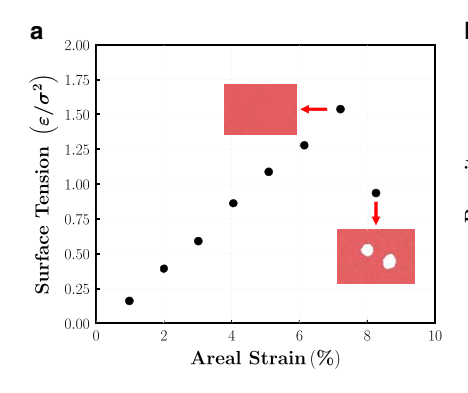


FIGURE 1 (a) Snapshot of the CGMD model of RBC membrane: lipid head, purple; lipid tail, dark blue; bolalipid head, red; bolalipid middle, light blue; cytoskeleton, green; junction points, yellow. (b) Top view of a membrane patch, (c) bottom view of a membrane patch, and (d) a slice of simulation box that shows half of a hydrophilic pore. To see this figure in color, go online.

employed the explicit-solvent model of Goetz and Lipowsky (31). This suggests that errors arising from this simplification are not significant for the pore formation on the membranes under extensional stress, and the implicit-solvent model is indeed modeling correct physical behavior. In our implementation of Cooke et al.'s (34) head-tail model, the cohesive range of tail particles is set to $w_c = 1.6\sigma$. The simulations are done at a temperature of $K_BT = 1.1\varepsilon$. At this temperature, the lipid bilayer in the presence of cytoskeleton has a fluid-like behavior with the diffusion constant of $0.007\sigma^2/\tau$, which is in the range of $\sim 0.01\sigma^2/\tau$ reported for headtail simulation of pure lipid bilayer (40). The thickness of lipid bilayer in our model is $\sim 5\sigma$. For the sake of clarity, the mapping between coarsegrained and real units will be discussed briefly. By comparing the thickness of the lipid bilayer in our simulation and typical experimental thickness of \sim 5 nm, the length unit can be estimated as $\sigma \approx 1$ nm. Moreover, considering the choice of $K_BT = 1.1\varepsilon$ and $K_BT = 4.1 \times 10^{-21} \text{ J} =$ 0.59 kcal/mol, the energy unit can be calculated as $\varepsilon = 0.54$ kcal/mol. By considering the molecular mass of a lipid molecule such as 1,2-dipalmitoyl-sn-glycero-3-phosphatidylcholine, which is 734 Da, the mass unit can be calculated as m = $(1/3) \times 734 \times 1.66 \times 10^{-27} = 4.06 \times 10^{-25}$ kg. Finding the time mapping is more challenging because various dynamic processes can be sped up differently as a result of coarse graining. A simple estimation of time unit based on energy (ε) , mass (m), and length units (σ) can be calculated by $\tau = \sigma \sqrt{(m/\varepsilon)} \approx 10.4$ ps. However, this mapping does not take into effect the faster dynamics of the coarsegrained system as a result of the significant reduction in degrees of freedom and molecular friction (41). Therefore, a speed-up factor should be multiplied in the time mapping to capture the real dynamics of the coarse-grained system. This speed-up factor can be calculated by comparing a physical value with similar observable in the CGMD simulation. We chose the diffusion process to estimate the speed-up factor because we believe that the diffusion coefficient of lipid molecules is highly effective on the growth and closure dynamics of nanoscale pores. The diffusion coefficient of various lipid molecules is reported in the range of $\sim 1 \,\mu \text{m}^2/\text{s}$ (57,58) which can be compared with the diffusion coefficient of $\sim 0.01\sigma^2/\tau$ from the simulations. Thus, the effective mapping of time units can be estimated as $\tau_{eff} \approx 10$ ns, which suggests a speed-up factor of \sim 1000. In the rest of this work, we use τ_{eff} as the time mapping of our model or τ . The Langevin thermostat with the friction coefficient of $\Gamma = \tau^{-1}$, the same unit mass for all particles, and a time step of $\delta t =$ 0.01τ is employed for all molecular dynamics (MD) simulations. In the unsteady simulations, each side of the computational box is deformed by the constant strain rate of $\mu(\tau^{-1})$, and the length of the simulation box at each time is $L = L_0(1 + \mu T)$, in which the L_0 and T are initial length and simulation time, respectively. Simulations are performed by the LAMMPS molecular dynamics package (59). The fix/deform function of

LAMMPS is used to stretch the computation box. It should be noted that in unsteady simulations, the velocity of particles as a result of box deformations is removed from the thermostatting process to ensure that the thermostat is applying only on thermal components of velocity, not their streaming velocity that comes from the stretching or compression process (60). Because of the periodicity of the cytoskeleton triangular meshwork, the length of the computational box is not the same in the x and y directions. The computation box size is $420\sigma \times 290\sigma \times 100\sigma$. All the geometries are equilibrated for 10⁶ steps in NPT (constant number of particles, constant pressure, constant temperature) ensemble with zero pressure to ensure the equilibrated and relaxed state of membrane before the loading process. The simulation box contains 666,721 particles with 446,144 bonds and 225,307 angles. Simulations are performed by XSEDE's SDSC Comet cluster with four to eight computational nodes (24 cores per node) with a computational performance of \sim 20–30 time steps per second. The simulation trajectory is visualized by the OVITO (61) package. To quantify pore characteristics, a surface mesh is created on the lipid bilayer surface. Then, the MATLAB (The MathWorks, Natick, MA) image processing module is used to measure the number and surface area of voided regions.

Finally, it is important to know the way that this model can be interpreted from a multiscale point of view. Deformations of RBCs in the flow can be modeled by a wide range of numerical approaches such as continuum-scale, finite-element (62,63), boundary-element (64), and mesoscale-particle-based methods (65). Sohrabi and Liu (5) developed a multiscale, strain-based damage model that couples the local strains at each patch of the cellular-scale RBC model with all-atomistic MD results of pore formation. In that approach, 5120 triangular elements are employed to model the RBC surface. Considering the surface area of \sim 135 μm² for the RBC, the area of each patch in their model can be approximated to be 2.64×10^{-14} m². On the other hand, the initial surface area of membrane patch in our model can be calculated as 12.18 \times 10^{-14} m², which is almost four times more than the element size of the cellular-scale model. Moreover, numerical simulations show that the stretching velocity of a patch at high shear rates, tank-treading motion, can reach to a few millimeters per second (5). However, the lowest stretching velocity in all-atomistic MD simulations is \sim 100 mm/s (21,23,25), which results in unrealistically high critical strains. Considering the strain rate of $10^{-5}\tau^{-1}$, initial length of ~420 nm, and time mapping of $\tau \approx$ 10 ns, the stretching velocity in our model can be approximated as ~0.42 mm/s, which is closer to the physiological range of shear-induced deformation velocities in medical devices under large deformations and high shear rate regimes (5). Thus, our model could potentially be coupled with the cellular-scale simulation approaches to predict the RBC damage in medical devices.



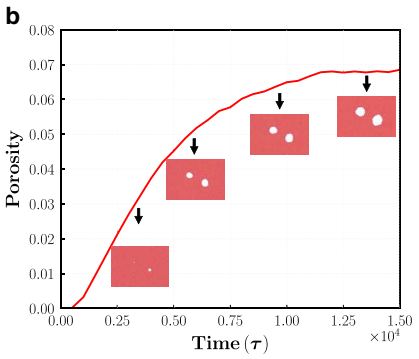


FIGURE 2 (a) Bilayer surface tension during the quasistatic stretching of the pure lipid bilayer and (b) pore growth during the equilibration at 8.3% areal strain. To see this figure in color, go online.

RESULTS AND DISCUSSION

To validate our CGMD model in terms of pore formation, we started with quasistatic simulations of a pure lipid membrane patch. In these simulations, the patch size is increased during stepwise deformation with the strain rate of $10^{-5}\tau^{-1}$ for 500τ , followed by a long-time, $10^4\tau$ equilibration simulation (with $\tau \approx 10$ ns, the equilibration time is ~ 0.1 ms) in the NVT (constant number of particles, volume, and temperature) ensemble. The areal strain, ε , can be defined as $\varepsilon =$ $(l_x l_y / l_{x0} l_{y0}) - 1$, in which the l and l_0 are the current length and initial length in the x and y direction, respectively. Fig. 2 a shows the results for the equilibrium surface tension after each deformation step of the patch. The critical strain is between 7.2 and 8.3% areal strain. The bilayer lateral tension $\Sigma = -l_z(p_{xx} + p_{yy})/2$, in which p_{xx} and p_{yy} are pressure in the x and y directions, respectively, is measured at various strains. At areal strain of 7.2%, the bilayer tension is $\sim 1.55(\varepsilon/\sigma^2)$. After this critical value, the membrane relaxes, and surface tension decreases with the formation of pores. Considering $K_BT = 1.1\varepsilon = 4.1$ pn • nm and $\sigma = 1$ nm, the critical surface tension is ~5.8 mN/m, which is close to the experimental results of 3–4 mN/m (42). Long-time equilibration just after the initial pore formation results in the formation of two stable, large pores with the average radius of \sim 37 nm on the membrane, as shown in Fig. 2 b. To quantify the pore area, we define porosity as $P = A_{pore}/$ A_0 , in which A_{pore} and A_0 are the total pore area and initial surface area of the patch before deformation, respectively. The final porosity in this case is ~ 0.068 , which means that the total pore area is about 6.8% of the initial surface area. Fig. 2 b also shows that it takes around $1.3 \times 10^4 \tau$ or 0.13 ms from pore formation to grow to a stable size, which is significantly long compared to the rate of deformation of RBC under high shear flow. In later sections, we will consider this dynamic pore formation process through nonequilibrium simulations.

Effects of cytoskeleton on pore formation

The simulations so far only considered the lipid bilayer, whereas the real RBC membrane has a cytoskeleton, i.e., spectrin network, together with the lipid bilayer. The cytoskeleton largely increases the mechanical strength of the membrane, yet its influence on pore formation and cell damage is unknown. To analyze the effects of the cytoskeleton on the formation and growth of pores, three different cases are studied: one lipid bilayer without cytoskeleton (WO) and two lipid bilayers coupled to the cytoskeletons with $JD = 80\sigma$ (D80, similar to the JD of real RBCs) and $JD = 40\sigma$ (D40, an artificial case with denser JD to check out what happens to pore formation if cytoskeleton density is doubled). A strain rate of $10^{-5}\tau^{-1}$ ($\sim 1000 \text{ s}^{-1}$) is applied equibiaxially in the x and y directions. The patches are stretched from the equilibrated, relaxed state to the areal strain of 15%. To find the critical areal strain, three simulations are performed for each geometry, and the average areal strain of pore formation is plotted in Fig. 3 a. The critical areal strain for the unsteady stretching of the WO case is 8.7%, which is slightly higher than the quasistatic simulation results of the previous section. This difference might come from the strain rate effects in which the pore opens at higher critical strain under higher strain rates. In addition, the critical strain is 10.2 and 12.5% for the D80 and D40 cases, respectively. Therefore, the cytoskeleton structure increases the resistance of membrane against pore formations. This effect is more apparent for the D40 case with the denser cytoskeleton structure. Another important effect of the cytoskeleton is confining the pore formation and growth process. To study the effects of cytoskeleton on the pore characteristics, three simulations for each cytoskeleton structure were performed, and the average and standard deviations of results are displayed in Fig. 3, b-d. As shown in Fig. 3 b, the presence of cytoskeleton can reduce the porosity of the membrane patch under the same mechanical tension. In the WO case, the pores are free to grow with the diffusion of lipid molecules until the membrane tension is fully relaxed. However, in the D80 and D40 cases, the pores are confined by the cytoskeleton and its junction structures (transmembrane proteins). Therefore, under the same areal strain, the total pore area is smaller for the cases with cytoskeleton. Moreover, the density of pores in the membrane, which is defined by the number of pores divided by the initial surface area of the membrane patch (in micrometers

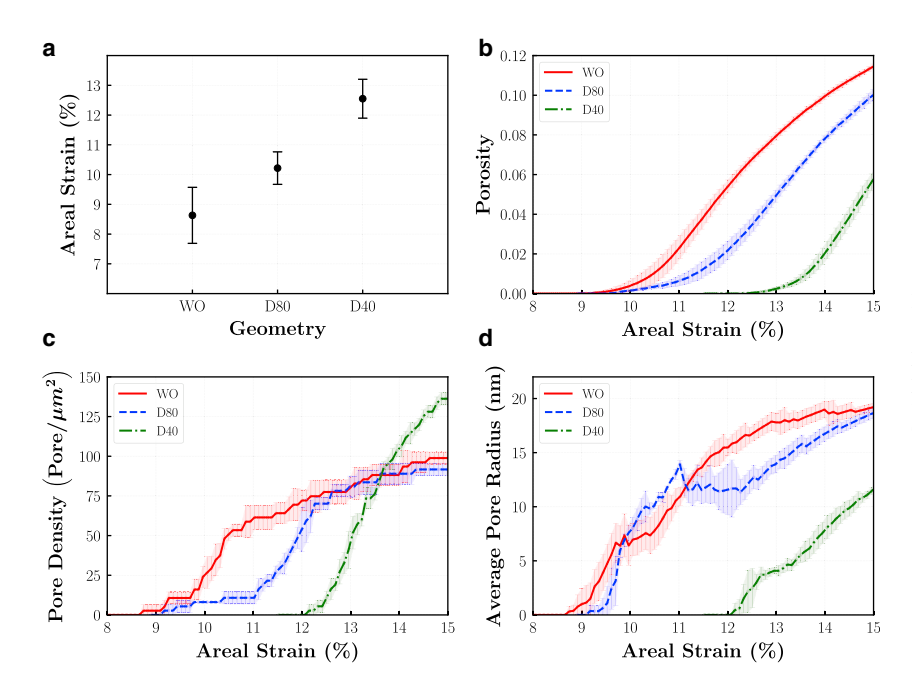


FIGURE 3 The influence of cytoskeleton on (a) the critical areal strain of pore formation, (b) membrane porosity, (c) membrane pore density, and (d) average pore radius. Error bars show standard deviations from the average value of three simulations for each case. To see this figure in color, go online.

squared), exhibits interesting behavior. As shown in Fig. 3 c, the density of pores slightly decreases by adding the cytoskeleton (D80), yet it increases when the denser cytoskeleton is used (D40). This behavior of the D40 case can be explained by the energetics of pores during growth. In the presence of dense cytoskeleton, it is very hard for the already formed pores to pass through the cytoskeleton vertices, and the area of pores is limited to the cytoskeleton triangles. Thus, the formation of new pores becomes energetically more favorable than the growth of already formed pores; thus, the D40 case has lots of small pores leading to the highest pore density. In general, the process of transient pore formation and pore characteristics on the surface of the RBC membrane should be understood as an interplay among the lipid bilayer, cytoskeleton, and transmembrane proteins. As shown in Fig. 3 d, the average radius of pores decreases with the existence of cytoskeleton. Moreover, as a result of the formation of more pores in the D40 case, the average radius apparently decreases. Fig. S1 shows snapshots of pores in these three different cases at the areal strain of $\sim 14.5\%$.

The simulations above considered the initialization of pores from a perfect lipid membrane, which shows a critical strain well above the experimentally measured critical strain of 4% (27,28). The actual lipid membrane is under complex biophysiological conditions and consists of diffusive proteins that are likely to have various types of defects. To consider the influence of these defects, we also analyzed the critical strain of preformed pores (mimicking the defects), which can be defined as the areal strain in which the preformed pores do not reseal and start to grow. In these simulations, a pore with the radius of 5 nm is opened on a patch of D80 membrane that is stretched to the areal strains of 4, 5, and 6%. The initial location of the pore is chosen to be as far as possible from the cytoskeleton junctions to simulate the worst-case scenario, in which the growth of defects is not limited by the junction units. At each areal strain, an equilibrium CGMD simulation in the NAT ensemble is performed for 3.5×10^6 steps or ~ 0.35 ms to check the stability of pores. At the areal strain of 4%, the preformed pore is completely resealed during the NAT equilibration. However, at the areal strains of 5 and 6%, pores grow and reach the cytoskeleton junctions. Therefore, the critical strain is between 4 and 5%, which is close to the experimental critical areal strain, i.e., \sim 4% (27,28). Moreover, at the areal strain of 5 and 6%, the final, stable pores are limited by the cytoskeleton junctions. As a result, the stable pore radius is 33.70 and 39.74 nm for the areal strains of 5 and 6%, respectively (snapshots of pores are shown in Fig. 4). These results suggest that the low 4% critical areal strain observed in the experimental tests of blood cell damage might possibly be induced by the defects on the membrane. We also studied the effect of defect size on the critical strain of pore formation. Simulations are performed with the same simulation setup discussed before. The final outcome of stable pore formation or complete closure is analyzed for various defect radiuses in the range of 2–10 nm. As shown in Fig. 4, the critical strain of pore formation declines when the initial pore or defect radius is larger. However, even a pore with a radius of 10 nm is completely closed at the areal strain of 3%. On the other hand, by reducing the defect radius, the critical strain of pore formation increases and gets closer to the values that we reported before for healthy membranes (8–9%).

Moreover, in this work, the cytoskeleton is considered as a perfectly connected triangular network with a JD of

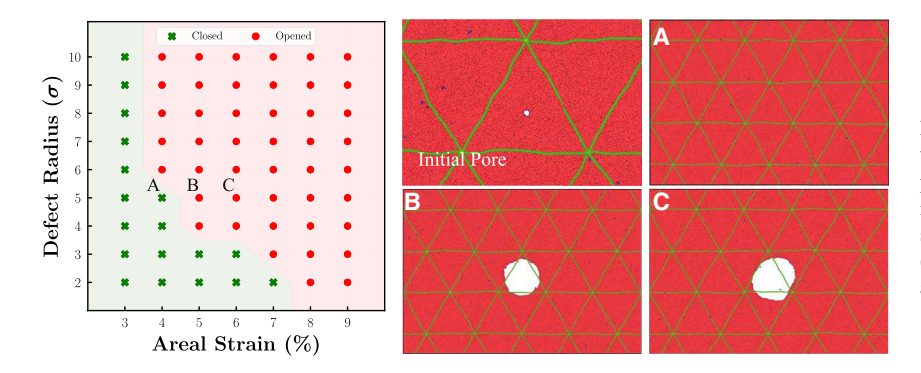


FIGURE 4 Effect of defect (initial pore) size on the final outcome of stable pore formation or complete recovery of the defect. Snapshots show the initial pore location and equilibration simulation results for a 5 nm pore at the areal strain of (A) 4% (the initial pore is completely resealed), (B) 5%, and (C) 6%. To see this figure in color, go online.

80 nm. However, in the real RBC, there are many defects and void spaces in the cytoskeleton structure that can reduce the critical strain of pore formation and pore growth (43). To our knowledge, this is the first study that reports coarsegrained molecular simulations that predict critical strain very close to experimental results. Prior CGMD studies reported critical strains that are a few times larger than experimental values (37,41).

Pore closure under relaxation and compression

RBCs experience complex dynamic load in medical devices. After the initial pore formation on the membrane surface, the pore might open bigger under larger loading or might reseal and close under relaxed loading or even compression. We studied the resealing mechanism by applying negative strain rates that recover the stretched patch. We limited our simulation only to the D80 case, which is similar to the real RBC. A negative strain rate of

 $-10^{-5}\tau^{-1}$ (-1000 s⁻¹) is applied equibiaxially on the computational box to model the load relaxation. The same simulation parameters used for pore formation are used for pore closure modeling. Three areal strains of 10.25, 12.5, and 14.75% are chosen to start the closure process. These cases are represented as closure 1, closure 2, and closure 3, respectively. As shown in Fig. 5 a, the total energy of the system increases during the stretching and drops after the initial pore opening. During the compression process, the surface tension decreases, and pores shrink. Fig. 5 b shows that the membrane porosity initially increases even under load relaxation. In other words, at the start of the compression, when the surface tension of the system is decreasing, the pores are still growing for a short period of time. This decrease in the surface tension while the area of pore is increasing (both are decreasing the system energy) results in a faster drop in the energy of the system. Because of this effect, the negative slope of the system energy (Fig. 5 c) is higher at the start of recovery process. The

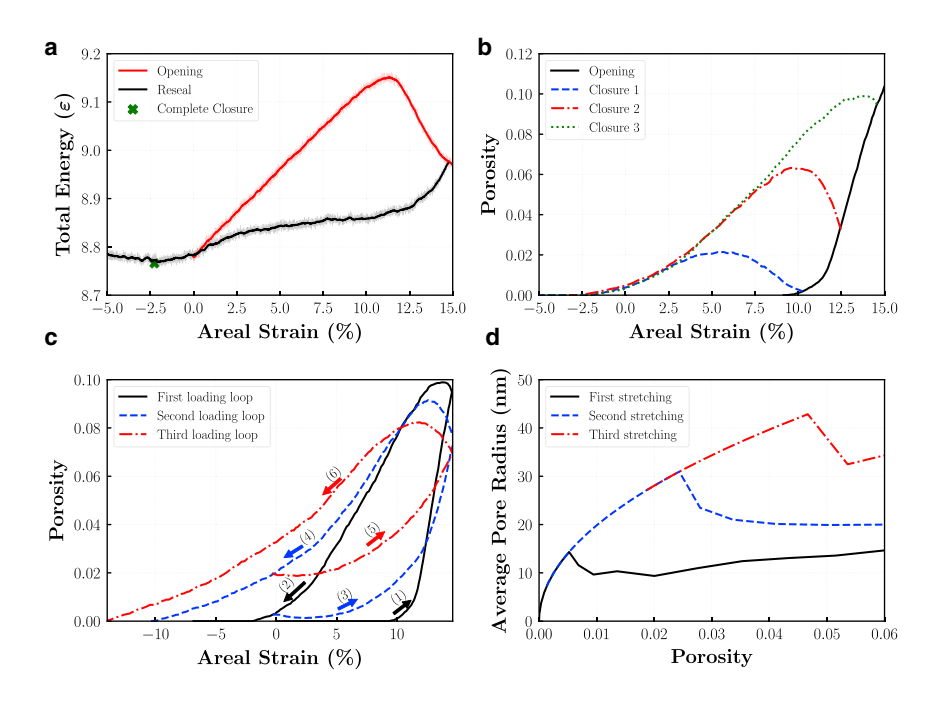


FIGURE 5 (a) Total energy of the system during pore opening and reseal, (b) porosity of membrane during reseal process under negative strain rate relaxation/compression, (c) porosity of membrane during three consecutive loading cycles, and (d) average pore radius versus membrane porosity during the stretching parts of three consecutive loading loops. To see this figure in color, go online.

reason for the initial increase in the porosity during the relaxation might be that the pores have not had enough time to grow during the stretching part. Thus, for the closure 3 case in which the pore has already grown more than other cases, the initial increase in the pore area is lower than other cases. After reaching a local maximum for the porosity that is different by starting from various areal strains, pores start to shrink. The trend of porosity over strain after this point is almost similar for all three cases. Another interesting behavior during the unsteady closure simulations is that the pores do not close at the same critical strain that they opened. Although the pores open at the critical strain of \sim 9.4%, they never close at positive strains during the closure with the same but negative strain rate. Our unsteady pore closure simulations show that pores can remain open during the relaxation process until the areal strain of \sim 2.2% (Fig. 5 a). Therefore, in a cyclic loading condition in which the areal strain increases and decreases periodically, the pores might remain open during the whole process when the areal strain is not negative.

Such a cyclic loading process can happen during the RBC tank-treading motion under high shear rates. An example of the tank-treading motion and local areal strains on the surface of an RBC is displayed in Fig. S2. Although patches on the RBC surface experience high positive areal strains during the tank-treading motion, the negative areal strains during the compression may not be enough to close all the open pores. Therefore, the open pores start to grow again during the next cycle, which leads to a larger pore area. To examine this effect, we simulated two more loading loops (stretching and compression) starting from an instance of the closure simulation explained above (closure 3 case), when the areal strain is almost zero. During the second loop, the patch is stretched again by the same positive, equibiaxial strain rate of $10^{-5}\tau^{-1}$, followed by another compression simulation with the same negative strain rate starting from the areal strain of \sim 14.7%. As shown in Fig. 5 c, during the second and third loop, pores that are still open start to grow again after a slight decrease in porosity as a result of previous unsteady compression. At the areal strain of \sim 14.7%, the porosity of the second and third cycles is lower than the first one. This can be explained by the fact that there is not any energy barrier for the pore formation during the second loop because the pores are already formed during the previous cycle. Thus, less pore area is needed to relax the system energy. On the other hand, as plotted in Fig. 5 c, there is a large difference between the areal strain of complete closure (when porosity reaches zero again) during the first and next loading cycles. Whereas at the first loop, opened pores close completely at the areal strain of -2.2%, during the second and third cycles, complete resealing happens at -10.0 and -14.1%, respectively. The reason for this difference is that the average pore radius is higher at the start of the second compression phase than the first one because the open pores at the end of the first cycle have more time to grow during the next loading cycles. Fig. 5 d shows the average pore radius during the stretching phase of the first and next loading cycles. At the same porosity, the second and third loops have higher average pore radiuses. Therefore, during the compression phase, higher energy is needed to reseal the larger pores, which results in more negative areal strains required for complete pore resealing. Fig. S3 shows snapshots of membrane during the compression parts of loading cycles. It can be seen that at the end of each stretching part (or the start point of the recovery process), there are a smaller number of pores with larger radius in comparison with the same point at the previous cycle. Therefore, cyclic loading leads to a smaller number of larger pores that are harder to reseal and more dangerous for the membrane. This can qualitatively explain the effect of exposure time on the hemolysis of RBCs, in which the total amount of damage can be related both to the amount of shear stress and the time that RBCs are under that stress condition (65). Higher exposure time, i.e., more loading cycles, transfers the high number of small transient pores into a small number of large and hard-to-recover pores that ultimately result in more RBC damage and hemoglobin release.

Complex loading conditions

The unsteady simulations of previous sections were performed in an equibiaxial way in which the strain rate is similar for x and y directions. However, a patch of RBC membrane under flow usually experiences more complex loading conditions that can be transferred into nonequal principal stresses. Here, for the sake of brevity, we just focus on the non-equibiaxial and strip biaxial loading conditions (Fig. S4 shows the schematics of various loading types). In the non-equibiaxial simulations, although the strain rate in the y direction is $10^{-5}\tau^{-1}$, the x direction strain rate is two or four times higher, which is shown as the NEQ2 or NEQ4 case, respectively. On the other hand, in the strip biaxial case, the strain rate in the y direction is fixed to zero, and the membrane is stretched only in the x direction by the strain rate of $10^{-5}\tau^{-1}$, which is shown as the ST case. Simulations of various loading conditions are performed on the D80 membrane, and the unsteady stretching process is continued until the point that the areal strain reaches 15%. Other simulation parameters are similar to the previous sections. Each simulation is repeated three times, and the average and standard deviations of results are shown in Fig. 6. The equibiaxial results are also plotted as the EQ case for better comparison. As shown in Fig. 6 a, the porosity of membrane for various cases decreases by increasing the complexity (from ST to NEQ4) of loading. The highest porosity is for the ST case. This can be explained by the longer simulation time that it needs to reach the same areal strain with others. Because the ST case has only one strain rate in the x direction, it requires more time than the EQ, NEQ2, and NEQ4 cases to reach the

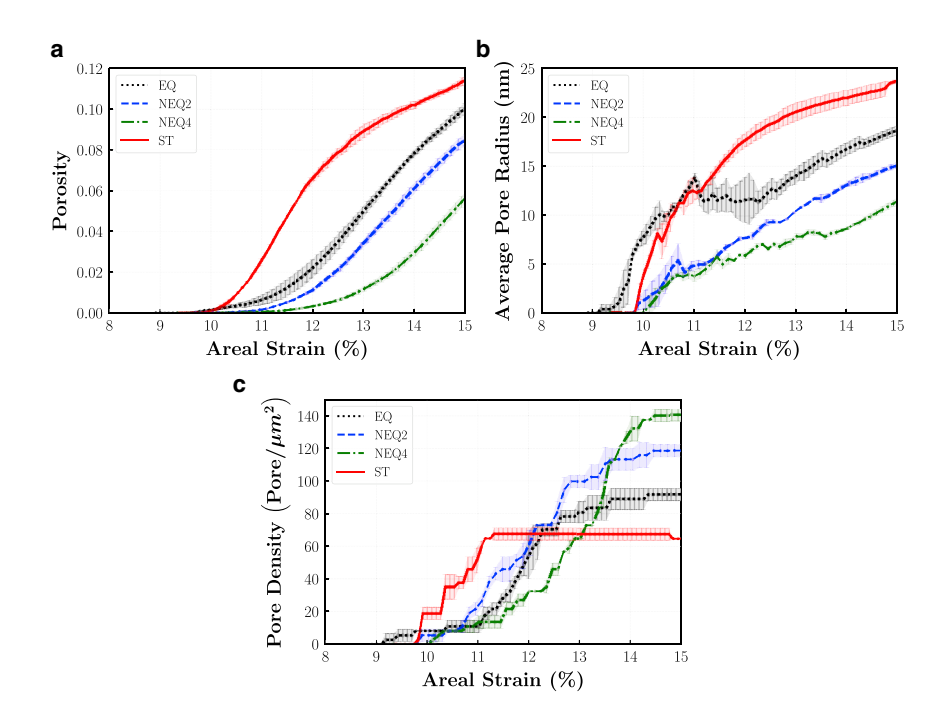


FIGURE 6 (a) Porosity versus areal strain, (b) average pore radius versus areal strain, and (c) pore density versus areal strain for various loading conditions. Error bars show standard deviations from the average value of three simulations for each case. To see this figure in color, go online.

same areal strain. Therefore, each pore has more time to diffuse and grow, which results in higher porosity and larger total pore area at the same areal strain. On the other hand, the NEO4 case reaches the 15% areal strain in less time than other cases. Thus, pores have less time to grow, which results in less total porosity. As shown in Fig. 6, b and c, although the critical strain rates are almost similar for all cases, the average pore radius decreases and pore density increases in more complex loading conditions. The most density of pores can be seen in the NEQ4 case, in which the pore density is more than twice of the ST case. This suggests that the lipid bilayer is not able to resist highly unequal, shearlike loading conditions, and new, smaller pores form more easily on the membrane surface in non-equibiaxial loading. Therefore, it can be concluded that more complex types of loading can significantly increase the number of pores, which leads to a lower average pore radius. This conclusion is in qualitative agreement with the all-atomistic simulations of Murphy et al. (24), which reported an increase in the density of pores in more complex loading conditions.

Effects of strain rate on pore formation and growth

Finally, we studied the influence of strain rate on the formation of pores. The time dependency of membrane disintegration has been reported both in experimental and computational studies. The micropipette aspiration experiments of Evans et al. (27) show that increasing the loading rate in the range of 0.01–100 mN/m results in higher critical rupture tensions for lipid vesicles. Li et al. (38) reported that RBCs can withstand the areal strain of ~40% under very high rate deformations generated by an impulse-like, laser-induced cavitation bubble (usually during a few tens of microseconds). This critical strain is one order of magnitude higher than the quasistatic critical strain of 2-5% (28,66). The same behavior is qualitatively reported in all-atomistic MD simulations (23,24,39). However, limited by the available computational resources, the all-atomistic results are usually performed in small patch sizes (a few tens of nanometers squared) and at very high strain rates in the range of $\sim 10^6 - 10^{10} \text{ s}^{-1}$, which are close to or even higher than the shock-wave-induced strain rates (22,37). This leads to the pulling speed in the range of few meters per second on a typically nanometer-scale patch. Meanwhile, the typical strain rate of 4000–42,000 s⁻¹ under a high shear flow of medical devices results in the pulling speeds in the range of a few millimeters per second, which is out of the reach of all-atomistic MD simulation in literature (5). Here, we focus on the strain rate effects in length- and timescales that are hardly accessible for all-atomistic MD. As a result, the pores are able to form and grow with less artificial effects arising from the finite-size effects and unrealistically high strain rates. The unsteady simulations are performed with equibiaxial stretching rates of $10^{-5}\tau^{-1}$, $5.0 \times 10^{-5}\tau^{-1}$, $10^{-4}\tau^{-1}$, and $5.0 \times 10^{-4} \tau^{-1}$ (considering the time unit of $\tau \approx 10$ ns, the strain rates are 10^3 , 5×10^3 , 10^4 , and 5×10^4 s⁻¹). Each case is repeated three times, and average values of critical strains are reported (the error bars show the standard deviation of results from the mean value). The same method as discussed for the pure lipid bilayer is utilized again to run the quasistatic simulation. The D80 membrane patch, which has the initial size of $420\sigma \times 290\sigma \times 100\sigma$

 $(420 \times 290 \times 100 \text{ nm})$, is used for all the simulations, and each simulation is continued to the point that porosity of membrane reaches the limit of P = 0.12 (total pore area is 12% of initial patch area). The critical strain of pore formation under various strain rates is plotted in Fig. 7 a. The quasistatic result is shown by the strain rate of zero. The critical areal strain increases by approximately 100% when the strain rate increases from $10^{-5}\tau^{-1}$ to 5 \times $10^{-4}\tau^{-1}$. The dependency of critical strain on the strain rate is less in lower strain rates but increases at higher rates. Fig. 7 b shows the porosity of membrane in various areal strains. It can be seen that although the critical strain is different, the pore growth over increased strain (the slope of porosity) is almost the same for all cases. The slope is slightly lower for the case of $5 \times 10^{-4} \tau^{-1}$ because of higher pore density, which limits the growth rate of each pore. In other words, after the initial pore formation, the growth rate of total pore area is similar for all cases. Multipore formation is also reported in AA MD simulations of higher stretching velocities (21,23). Although our large membrane patch can have more than one pore even in quasistatic simulations of areal strains larger than 9% (for the case without cytoskeleton at the areal strain of 8.3%, as shown in Fig. 2), employing higher strain rates dramatically increases the density of pores. As shown in Fig. 7 c, the density of pores under the strain rate of 5 \times $10^{-4}\tau^{-1}$ is approximately three times larger than the case with the strain rate of $10^{-4}\tau^{-1}$ under the same porosity. This jump in the pore density can be explained by the fact that the pores do not have enough time to grow at higher rates when the strain increases very fast and the membrane has to relax its energy by opening new pores. Fig. 7 d depicts the average pore radius at each porosity

for various high strain rate cases. As an obvious consequence of the higher pore density under the same porosity, the average pore radius is lower at higher strain rates. Snapshots of Fig. 7 c show membrane patches at the same porosity of P = 0.1 for various strain rates. Greater number and less average radius of pores at higher strain rates might be useful in drug loading applications, in which a specific total area of pore is achieved without making very large pores that grow unlimitedly and result in complete rupture and cell lysis. In contrast, lower strain rates are favorable for generating larger pores that allow loading of large molecules that cannot easily pass through small pores.

CONCLUSION

We have developed a CGMD model for the RBC membrane with a triangular meshwork of CG beads that represents the cytoskeleton structure to analyze the process of formation, growth, and closure of transient pores. The presence of cytoskeleton and transmembrane proteins limits the pore growth, which results in a lower total pore area. Moreover, a critical areal strain between 4 and 5% for pore growth is observed with consideration of membrane defects, which is consistent with experimentally measured critical strain of \sim 4% (27,28). This suggests that defects might be one of the reasons for the discrepancy that is observed between the critical strain of pore formation in numerical modeling and experiments. The process of pore recovery under negative strain rates is also studied. The closure process of pores is not the same as the opening. Pores remain open until negative areal strains of \sim 2%, suggesting that once a pore forms on the

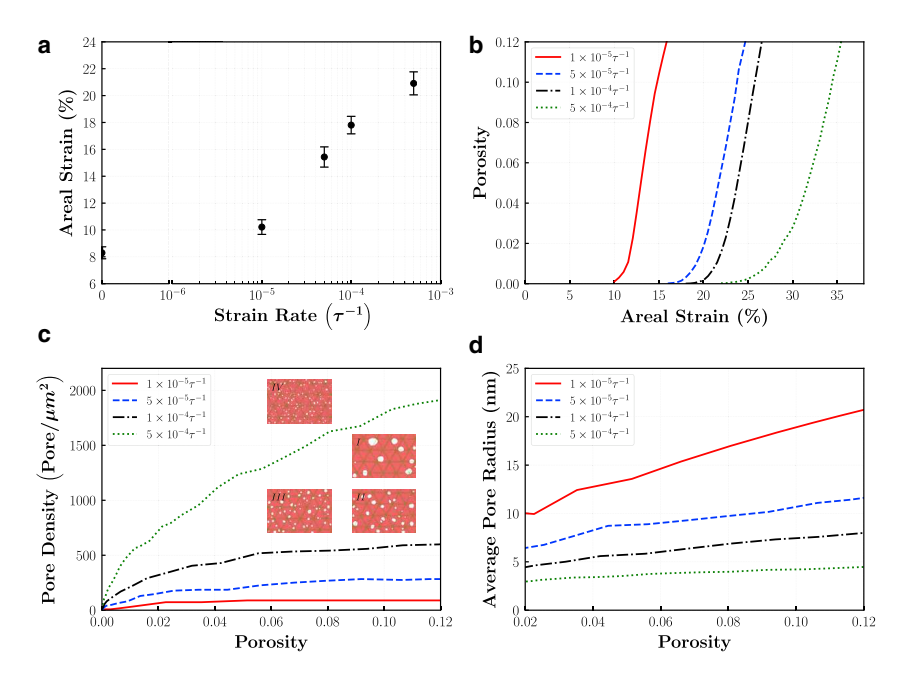


FIGURE 7 (a) Critical strain of membrane (error bars show standard deviations from the average value of three simulations for each case), (b) porosity of membrane versus areal strain, (c) density of pores versus porosity (snapshots I-IV show the pore numbers at the porosity of P = 0.1 for 1×10^{-5} $5 \times 10^{-4} (\tau^{-1})$, respectively), and (d) average radius of pores versus porosity for various strain rates. To see this figure in color, go online.

membrane, it might remain open until the local areal strain reaches negative values. Similar cyclic loading conditions can be experienced by RBCs that have tank-treading motion under high shear rate flows. The cyclic loading of a patch can lead to a lower number of pores with a larger radius that require more energy to recover again. Moreover, we analyzed non-equibiaxial and strip biaxial cases to study the effect of more complex loading conditions on the pore formation process. Although the critical strain is not very sensitive to these changes, the porosity and average pore radius decreases when the patch experiences more complex loading conditions. Moreover, the pore density increases in non-equibiaxial cases. Utilizing this mesoscale CGMD model, we studied the effect of higher stretching rates in the pore formation process. Thanks to the computational gains of employing an implicit-solvent CGMD model, we can simulate much larger patches than all-atomistic MD simulations that alleviate finite-size effects under more realistic, lower strain rates. In agreement with experimental and computational studies at various length scales, the critical strain increases with higher strain rates. Furthermore, the density of pores increases at higher strain rates. Despite all the simplifications, this CGMD model provides new, to our knowledge, insights into the process of transient pore formation in the RBC membrane. Moreover, considering the multiscale nature of the RBC pore formation during damage or drug delivery, this model can be employed as a finer-scale tool that can be coupled with continuum, cellular-scale models and predict the pore characteristics based on the local strains on the membrane surface. Further development of this model, including a more complex representation of cytoskeleton and transmembrane protein, is currently under progress.

SUPPORTING MATERIAL

Supporting Material can be found online at https://doi.org/10.1016/j.bpj. 2020.06.016

AUTHOR CONTRIBUTIONS

M.R. designed research, performed research, analyzed data, and wrote the manuscript. M.N. and R.P. performed research, analyzed data, and wrote the manuscript. Y.L. designed and directed research, performed research, analyzed data, and wrote the manuscript.

ACKNOWLEDGMENTS

The authors acknowledge the support of this work from the National Institutes of Health grant R01HL131750. This work used the Extreme Science and Engineering Discovery Environment through allocation MCB180032.

SUPPORTING CITATIONS

References (67,68) appear in the Supporting Material.

REFERENCES

- 1. Sharei, A., J. Zoldan, ..., K. F. Jensen. 2013. A vector-free microfluidic platform for intracellular delivery. Proc. Natl. Acad. Sci. USA. 110:2082-2087.
- 2. Stewart, M. P., R. Langer, and K. F. Jensen. 2018. Intracellular delivery by membrane disruption: mechanisms, strategies, and concepts. Chem. Rev. 118:7409-7531.
- 3. Stewart, M. P., A. Sharei, ..., K. F. Jensen. 2016. In vitro and ex vivo strategies for intracellular delivery. Nature. 538:183–192.
- 4. Blackshear, P. L., and R. J. Anderson. 1977. Hemolysis thresholds in microporous structures. In Red Cell Rheology, Volume 3. M. Bessis, S. B. Shohet, and N. Mohandas, eds.. Springer, pp. 377-395.
- 5. Sohrabi, S., and Y. Liu. 2017. A cellular model of shear-induced hemolysis. Artif. Organs. 41:E80-E91.
- 6. Faghih, M. M., and M. K. Sharp. 2019. Modeling and prediction of flow-induced hemolysis: a review. Biomech. Model. Mechanobiol. 18:845-881.
- 7. Nikfar, M., M. Razizadeh, ..., Y. Liu. 2020. Prediction of mechanical hemolysis in medical devices via a Lagrangian strain-based multiscale model. Artif Organs In press. Published online February 3, 2020. https://doi.org/10.1111/aor.13663.
- 8. Nikfar, M., M. Razizadeh, ..., Y. Liu. 2020. Multiscale modeling of hemolysis during microfiltration. Microfluid. Nanofluidics. 24:33.
- 9. Leverett, L. B., J. D. Hellums, ..., E. C. Lynch. 1972. Red blood cell damage by shear stress. Biophys. J. 12:257-273.
- 10. Yu, H., S. Engel, ..., D. Thévenin. 2017. A review of hemolysis prediction models for computational fluid dynamics. Artif Organs.
- 11. Giersiepen, M., L. J. Wurzinger, ..., H. Reul. 1990. Estimation of shear stress-related blood damage in heart valve prostheses-in vitro comparison of 25 aortic valves. Int. J. Artif. Organs. 13:300-306.
- 12. Okamoto, E., T. Hashimoto, ..., Y. Mitamura. 2003. Blood compatible design of a pulsatile blood pump using computational fluid dynamics and computer-aided design and manufacturing technology. Artif. Organs. 27:61-67.
- 13. Arora, D., M. Behr, and M. Pasquali. 2004. A tensor-based measure for estimating blood damage. Artif. Organs. 28:1002-1015.
- 14. Arora, D., M. Behr, and M. Pasquali. 2006. Hemolysis estimation in a centrifugal blood pump using a tensor-based measure. Artif. Organs. 30:539-547.
- 15. Vitale, F., J. Nam, ..., M. Pasquali. 2014. A multiscale, biophysical model of flow-induced red blood cell damage. AIChE J. 60:1509–1516.
- 16. Bavi, N., Y. Nakayama, ..., B. Martinac. 2014. Biophysical implications of lipid bilayer rheometry for mechanosensitive channels. Proc. Natl. Acad. Sci. USA. 111:13864-13869.
- 17. Martinac, A. D., N. Bavi, ..., B. Martinac. 2017. Pulling MscL open via N-terminal and TM1 helices: a computational study towards engineering an MscL nanovalve. PLoS One. 12:e0183822.
- 18. Tieleman, D. P., H. Leontiadou, ..., S. J. Marrink. 2003. Simulation of pore formation in lipid bilayers by mechanical stress and electric fields. J. Am. Chem. Soc. 125:6382-6383.
- 19. Leontiadou, H., A. E. Mark, and S. J. Marrink. 2004. Molecular dynamics simulations of hydrophilic pores in lipid bilayers. Biophys. J. 86:2156-2164.
- 20. Bennett, W. F. D., and D. P. Tieleman. 2011. Water defect and pore formation in atomistic and coarse-grained lipid membranes: pushing the limits of coarse graining. J. Chem. Theory Comput. 7:2981-2988.
- 21. Koshiyama, K., and S. Wada. 2011. Molecular dynamics simulations of pore formation dynamics during the rupture process of a phospholipid bilayer caused by high-speed equibiaxial stretching. J. Biomech. 44:2053-2058.
- 22. Bennett, W. F. D., N. Sapay, and D. P. Tieleman. 2014. Atomistic simulations of pore formation and closure in lipid bilayers. Biophys. J. 106:210-219.

- 23. Shigematsu, T., K. Koshiyama, and S. Wada. 2015. Effects of stretching speed on mechanical rupture of phospholipid/cholesterol bilayers: molecular dynamics simulation. Sci. Rep. 5:15369.
- 24. Murphy, M. A., M. F. Horstemeyer, ..., R. Prabhu. 2016. Nanomechanics of phospholipid bilayer failure under strip biaxial stretching using molecular dynamics. Model. Simul. Mater. Sci. Eng. 24:055008.
- 25. Bakhtiarydavijani, A., M. A. Murphy, ..., R. K. Prabhu. 2019. Damage biomechanics for neuronal membrane mechanoporation. Model. Simul. Mater. Sci. Eng. 27:065004.
- 26. Zhang, L., Z. Zhang, ..., A. Jérusalem. 2019. Molecular dynamics simulation of cell membrane pore sealing. Extreme Mech. Lett. 27:83-93.
- 27. Evans, E., V. Heinrich, ..., W. Rawicz. 2003. Dynamic tension spectroscopy and strength of biomembranes. Biophys. J. 85:2342–2350.
- 28. Evans, E. A., R. Waugh, and L. Melnik. 1976. Elastic area compressibility modulus of red cell membrane. Biophys. J. 16:585-595.
- 29. Marrink, S. J., A. H. De Vries, and A. E. Mark. 2004. Coarse grained model for semiquantitative lipid simulations. J. Phys. Chem. B. 108:750-760.
- 30. Smit, B., K. Esselink, ..., I. Szleifer. 1993. Computer simulations of surfactant self-assembly. Langmuir. 9:9-11.
- 31. Goetz, R., and R. Lipowsky. 1998. Computer simulations of bilayer membranes: self-assembly and interfacial tension. J. Chem. Phys. 108:7397-7409.
- 32. Drouffe, J. M., A. C. Maggs, and S. Leibler. 1991. Computer simulations of self-assembled membranes. Science. 254:1353-1356.
- 33. Wang, Z. J., and D. Frenkel. 2005. Modeling flexible amphiphilic bilayers: a solvent-free off-lattice Monte Carlo study. J. Chem. Phys.
- 34. Cooke, I. R., K. Kremer, and M. Deserno. 2005. Tunable generic model for fluid bilayer membranes. Phys. Rev. E Stat. Nonlin. Soft Matter Phys. 72:011506.
- 35. Neder, J., B. West, ..., F. Schmid. 2010. Coarse-grained simulations of membranes under tension. J. Chem. Phys. 132:115101.
- 36. Tolpekina, T. V., W. K. den Otter, and W. J. Briels. 2004. Nucleation free energy of pore formation in an amphiphilic bilayer studied by molecular dynamics simulations. J. Chem. Phys. 121:12060-12066.
- 37. Tolpekina, T. V., W. K. den Otter, and W. J. Briels. 2004. Simulations of stable pores in membranes: system size dependence and line tension. J. Chem. Phys. 121:8014-8020.
- 38. Li, F., C. U. Chan, and C. D. Ohl. 2013. Yield strength of human erythrocyte membranes to impulsive stretching. Biophys. J. 105:872-879.
- 39. Zhang, L., Z. Zhang, ..., A. Jérusalem. 2017. Molecular dynamics simulations of heterogeneous cell membranes in response to uniaxial membrane stretches at high loading rates. Sci. Rep. 7:8316.
- 40. Cooke, I. R., and M. Deserno. 2005. Solvent-free model for self-assembling fluid bilayer membranes: stabilization of the fluid phase based on broad attractive tail potentials. J. Chem. Phys. 123:224710.
- 41. Deserno, M. 2009. Mesoscopic membrane physics: concepts, simulations, and selected applications. Macromol. Rapid Commun. 30:752-
- 42. Kwok, R., and E. Evans. 1981. Thermoelasticity of large lecithin bilayer vesicles. *Biophys. J.* 35:637–652.
- 43. Evans, E., and W. Rawicz. 1990. Entropy-driven tension and bending elasticity in condensed-fluid membranes. Phys. Rev. Lett. 64:2094-
- 44. Pan, L., R. Yan, ..., K. Xu. 2018. Super-resolution microscopy reveals the native ultrastructure of the erythrocyte cytoskeleton. Cell Rep. 22:1151-1158.
- 45. Li, H., and G. Lykotrafitis. 2014. Erythrocyte membrane model with explicit description of the lipid bilayer and the spectrin network. Biophys. J. 107:642-653.

- 46. Yuan, H., C. Huang, ..., S. Zhang. 2010. One-particle-thick, solventfree, coarse-grained model for biological and biomimetic fluid membranes. Phys. Rev. E Stat. Nonlin. Soft Matter Phys. 82:011905.
- 47. Li, H., H. Y. Chang, ..., G. Lykotrafitis. 2018. Modeling biomembranes and red blood cells by coarse-grained particle methods. Appl. Math. Mech. 39:3-20.
- 48. Fu, S. P., Z. Peng, ..., Y. N. Young. 2017. Lennard-Jones type pair-potential method for coarse-grained lipid bilayer membrane simulations in LAMMPS. Comput. Phys. Commun. 210:193-203.
- 49. Tang, Y. H., L. Lu, ..., G. E. Karniadakis. 2017. OpenRBC: a fast simulator of red blood cells at protein resolution. Biophys. J. 112:2030-
- 50. Spangler, E. J., C. W. Harvey, ..., M. Laradji. 2011. Computer simulation of cytoskeleton-induced blebbing in lipid membranes. Phys. Rev. E Stat. Nonlin. Soft Matter Phys. 84:051906.
- 51. Gao, X., T. Yue, ..., X. Zhang. 2017. Erythrocyte membrane skeleton inhibits nanoparticle endocytosis. AIP Adv. 7:065303.
- 52. Sikder, M. K. U., K. A. Stone, ..., M. Laradji. 2014. Combined effect of cortical cytoskeleton and transmembrane proteins on domain formation in biomembranes. J. Chem. Phys. 141:054902.
- 53. Ursitti, J. A., and J. B. Wade. 1993. Ultrastructure and immunocytochemistry of the isolated human erythrocyte membrane skeleton. Cell Motil. Cytoskeleton. 25:30–42.
- 54. Byers, T. J., and D. Branton. 1985. Visualization of the protein associations in the erythrocyte membrane skeleton. Proc. Natl. Acad. Sci. USA. 82:6153-6157.
- 55. Lux, S. E., IV 2016. Anatomy of the red cell membrane skeleton: unanswered questions. Blood. 127:187-199.
- 56. Han, B., R. Zhou, ..., X. Zhuang. 2017. Structural organization of the actin-spectrin-based membrane skeleton in dendrites and soma of neurons. Proc. Natl. Acad. Sci. USA. 114:E6678-E6685.
- 57. Pincet, F., V. Adrien, ..., D. Tareste. 2016. FRAP to characterize molecular diffusion and interaction in various membrane environments. PLoS One. 11:e0158457.
- 58. Machán, R., and M. Hof. 2010. Lipid diffusion in planar membranes investigated by fluorescence correlation spectroscopy. Biochim. Biophys. Acta. 1798:1377-1391.
- 59. Plimpton, S. 1995. Fast parallel algorithms for short-range molecular dynamics. J. Comput. Phys. 117:1-19.
- 60. Daivis, P. J., and B. D. Todd. 2006. A simple, direct derivation and proof of the validity of the SLLOD equations of motion for generalized homogeneous flows. J. Chem. Phys. 124:194103.
- 61. Stukowski, A. 2010. Visualization and analysis of atomistic simulation data with OVITO-the open visualization tool. Model. Simul. Mater. Sci. Eng. 18:015012.
- 62. Liu, Y., and W. K. Liu. 2006. Rheology of red blood cell aggregation by computer simulation. J. Comput. Phys. 220:139-154.
- 63. Zhang, L., A. Gerstenberger, ..., W. K. Liu. 2004. Immersed finite element method. Comput. Methods Appl. Mech. Eng. 193:2051–2067.
- 64. Pozrikidis, C. 2005. Numerical simulation of cell motion in tube flow. Ann. Biomed. Eng. 33:165-178.
- 65. Fedosov, D. A., B. Caswell, and G. E. Karniadakis. 2010. A multiscale red blood cell model with accurate mechanics, rheology, and dynamics. Biophys. J. 98:2215-2225.
- 66. Needham, D., and R. S. Nunn. 1990. Elastic deformation and failure of lipid bilayer membranes containing cholesterol. Biophys. J. 58:997-
- 67. Weik, F., R. Weeber, ..., C. Holm. 2019. ESPResSo 4.0 an extensible software package for simulating soft matter systems. Eur. Phys. J. Spec. *Top.* 227:1789–1816.
- 68. Cimrák, I., M. Gusenbauer, and I. Jančigová. 2014. An ESPResSo implementation of elastic objects immersed in a fluid. Comput. Phys. Commun. 185:900-907.